Energy dependence of the spatial distribution of inelastically scattered electrons in backscatter electron diffraction

Farangis Ram and Marc De Graef

The Energy Dependence of the Spatial Distribution

of Inelastically Scattered Electrons

in Back-Scatter Electron Diffraction

Farangis Ram[*] and Marc De Graef[†]

Carnegie Mellon University

Department of Materials Science and Engineering

5000 Forbes Ave. Pittsburgh, PA 15217

(Dated: March 26, 2018)

Abstract

In an Electron Back-Scatter Diffraction pattern (EBSP), the angular distribution of back-scattered electrons (BSEs) depends on their energy. Monte Carlo modeling of their depth and energy distributions suggests that the highest energy BSEs are more likely to hit the bottom of the detector than the top. In this paper, we examine experimental EBSPs to validate the modeled angular BSE distribution. To that end, the Kikuchi bandlet method is employed to measure the width of Kikuchi bands in both modeled and measured EBSPs. The results show that in an EBSP obtained with a $15\,\mathrm{keV}$ primary probe, the width of a Kikuchi band varies by about $0.4°$ from the bottom of the EBSD detector to its top. The same is true for a simulated pattern that is composed of BSEs with $5\,\mathrm{keV}$ to $15\,\mathrm{keV}$ energies, which validates the Monte Carlo simulations.

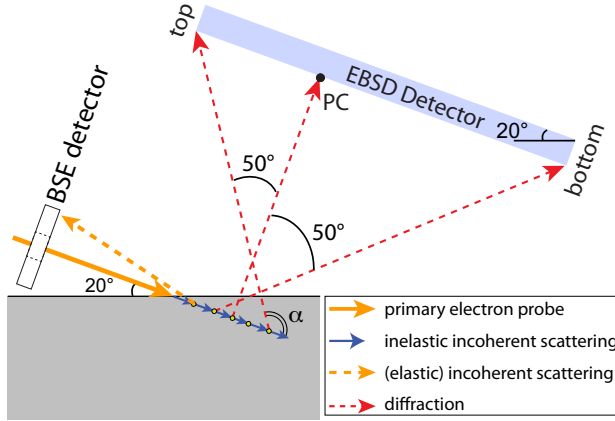**PACS numbers:** \pacs{68.37.Hk, 68.49.Jk, 61.05.J-}

FIG. 1. Electron Back-Scattering geometry in a Scanning Electron Microscope. α is the scattering angle and PC the pattern center.

When a coherent monochromatic electron beam, generated in a scanning electron microscope (SEM), enters a crystalline solid at a relatively shallow angle with respect to the sample surface (about 20°), the beam electrons interact with the crystal lattice and scatter in every direction (fig. 1). Both elastic and inelastic scattering events occur, and the electrons typically lose energy and change their trajectories multiple times inside the solid. Some of the electrons that back-scatter and leave the sample with very large scattering angles (> 170°) reach a detector mounted around the microscope's objective lens. Since back-scattered electrons (BSEs) are generated through Rutherford scattering from the atomic nuclei, BSE images obtained with this detector contain elemental information (Z-contrast). On the other hand, BSEs that leave the sample with scattering angles in the range [20°, 120°] are intercepted by an Electron Back-Scatter Diffraction (EBSD) detector and generate an electron back-scatter pattern (EBSP).

An EBSP consists of a smooth intensity background upon which a pattern of Kikuchi bands is superimposed. Each Kikuchi band (or K-band) represents a set of parallel lattice planes in a unit cell. If all the BSEs that comprise an EBSP had the same energy, then the edges of a K-band would correspond to the intersection of the Kossel cones of that energy on either side of the lattice plane with the detector plane. The opening angle of this right cone will be close to the Bragg angle. This means that on the Kikuchi sphere every K-band would have a constant width—except near low-index poles where dynamical scattering effects become important and the intensity profile is not simply the superposition

2

of the individual K-band profiles.

Assuming the width of a Kikuchi band is constant is the basis of a few methods that are aimed at improving the accuracy of the retrieved diffraction geometry[1–3]. Knowing the geometry of diffraction with a high accuracy is essential for extracting the stored elastic deformation[4,5] from an EBSP[6].

Physics-based modeling of EBSPs was first introduced by Winkelmann *et al.*[7]. EBSPs were originally modeled by making two simplifying assumptions: first, the BSEs that comprise the EBSP have a single energy equal to the energy of the primary probe; and second, these single-energy BSEs are angularly (spatially) uniformly distributed. EBSPs modeled using this approach very closely resemble the observed patterns. In these EBSPs, away from low-index poles, a K-band's width is constant, a fact that has been shown by Ram *et al.*[8] and will be verified here.

In reality, however, BSEs that make up an EBSP do not have the same energy; they have a range of energies. The exit direction of a BSE depends on its energy. In this paper we examine the energy dependence of the angular distribution of BSEs and show how it causes the width of a K-band to vary significantly and systematically over a measured EBSP.

The energy and spatial distributions of the BSEs can be modeled using Monte Carlo (MC) methods[9]. Each incident electron starts with the same energy, and travels into the solid. After a randomly chosen distance scaled by the mean free path length, the electron undergoes a Rutherford scattering event and changes its direction based on a random sampling of the angular part of the differential scattering cross section. In the simplest MC approach, the electron loses energy at a constant rate (Bethe's continuous slowing down approximation[10]). More realistic approaches incorporating discrete losses due to collective excitations and core-shell scattering events can be incorporated into the MC model, but the authors' experience shows that the final results are not very different from those of the simplified approach, except perhaps at the lowest energy losses due to collective excitations (e.g., plasmons). When an electron leaves the sample, two pieces of information are retained: the direction cosines of the trajectory after the last scattering event, and the electron's exit energy. A detailed discussion of the MC approach for EBSD pattern simulation can be found in Callahan and De Graef[11].

In fig. 2, the result of the Monte Carlo simulation of BSE formation is displayed for a Silicon sample. The energy of the primary probe is $E_{\rm p} = 15\,\mathrm{keV}$. The specimen plane and
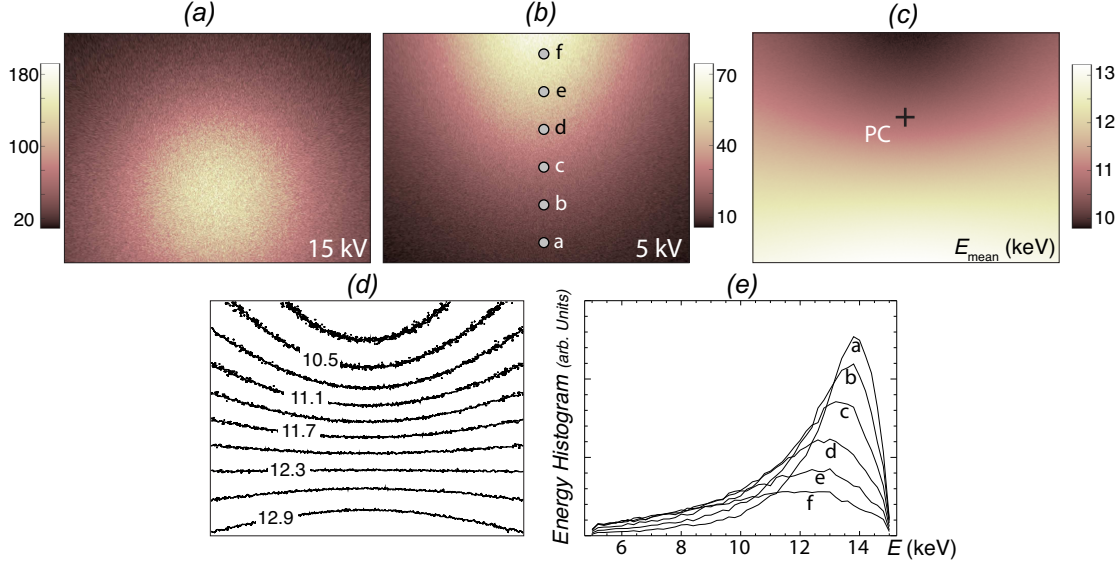
FIG. 2. Monte Carlo simulation of BSE formation.—BSE counts as a function of location on an EBSP for BSEs with: (a) 15 keV and (b) 5 keV energy. (c) Average BSE energy. (d) Contour plot of the average BSE energy in 0.3 keV steps. The primary probe energy is $E_\mathrm{p} = 15$ keV. (c) is composed of BSEs with 5 keV to 15 keV energies. The primary probe makes a 12° angle with the detector plane and a 70° angle with the specimen plane.

the camera plane make a 32° angle and the pattern center is marked by a cross. BSEs located at a vertical line that divides the pattern in two equal halves have scattering angles ranging from 20° to 110°.

Figure 2(a) and (b) show the modeled BSE counts for respectively 15 keV and 5 keV BSEs. They show that the angular distribution of BSEs is energy dependent. Most of the BSEs with larger energies reach the bottom of the detector (fig. 2(a)) while most of the BSEs with smaller energies arrive at the top of the detector (fig. 2(b)).

In fig. 2(c), the intensity of each pixel is equal to the arithmetic mean of the energies of all BSEs that reach that pixel. Included BSEs have 5 keV to 15 keV energies and the smallest difference in any two BSE energies is 0.2 keV. The contourplot of the mean energy is shown in fig. 2(d). Evidently, the model predicts that the mean BSE energy is about 3 keV larger at the bottom of the EBSP than at the top.

One way to examine the energy dependence of the angular distribution of BSEs is energy-filtering of the measured EBSP, such that only BSEs with a narrow energy range reach the EBSD detector. Energy-filtering can be achieved through adding an electrostatic energy

4

87 filter to a phosphor-CCD EBSD detector[12–14]. It can also be carried out digitally by using
88 a direct CMOS EBSD detector[15].

89 There is a second approach to examining the energy dependence of the angular distribu-
90 tion of BSEs. This approach does not need energy-filtering, and examines the width of the
91 Kikuchi bands over the EBSP. In this paper, we employ this second approach.

92 Figure 3(a) shows a measured EBSP generated by a 15 keV electron beam. In fig. 3(b) and
93 (c), two forward-modeled EBSPs with the same diffraction geometry as (a) are displayed.
94 The EBSP in (b) is created by BSEs with 5 keV to 15 keV energies. To model the EBSP in
95 (c), only BSEs with an energy larger than 14.8 keV were allowed to reach the detector.

96 The {220} Kikuchi band marked on fig. 3(c) is extracted from all three EBSPs using the
97 Kikuchi bandlet method[8]. The basis of the Kikuchi bandlet method is a high-level adaptive
98 geometrical dictionary that is built in the Fourier domain. More on high-level geometrical
99 dictionaries can be found in[16] for example. The Kikuchi bandlet method can deconvolute a
100 K-band of interest from all other K-bands that do not satisfy two conditions simultaneously:
101 (1) being parallel to the K-band of interest (2) spatially overlapping the K-band of interest.

102 The extracted K-bands are shown in fig. 3(d), (f), and (h). Intensity profiles of each
103 extracted K-band are obtained along the blue paths in (c). In each EBSP, path *1* is at the
104 bottom and path *19* is at the top of the EBSP. These paths are the intersections of great
105 circles that have their centers at the projection center (on the specimen surface) of the EBSP
106 and are perpendicular to the {220} lattice plane. The closest two paths on the EBSP are 4°
107 apart. For a detailed description of the retrieval of the intensity profiles,[8] can be consulted.

108 Intensity profiles for EBSPs displayed in fig. 3(a-c) are plotted in fig. 3(e), (g) and (i).
109 Profiles are plotted for EBSPs with two primary probe energies: E_p =15 keV in blue and
110 E_p =20 keV in red. The $E_p = 20$ keV EBSPs are not shown.

111 Examining the K-band intensity profiles of the two modeled EBSPs (fig. 3(g) and (i))
112 shows that each profile is approximately symmetric with respect to its center. Comparing
113 the corresponding intensity profiles (e.g. profile *11* in (g) and profile *11* in (i)) of the two
114 modeled EBSPs shows that the profiles are similar in their shape.

115 The intensity profiles of the measured EBSPs are different from the corresponding mod-
116 eled ones, however. For example, compare profile *11* in (e) and profile *11* in (g) and (i).
117 They are asymmetrical, not as smooth, and their variation along the K-band (compare pro-
118 file *5* and profile *15* in fig. 3(e)) is more pronounced. The asymmetry or the excess-deficiency
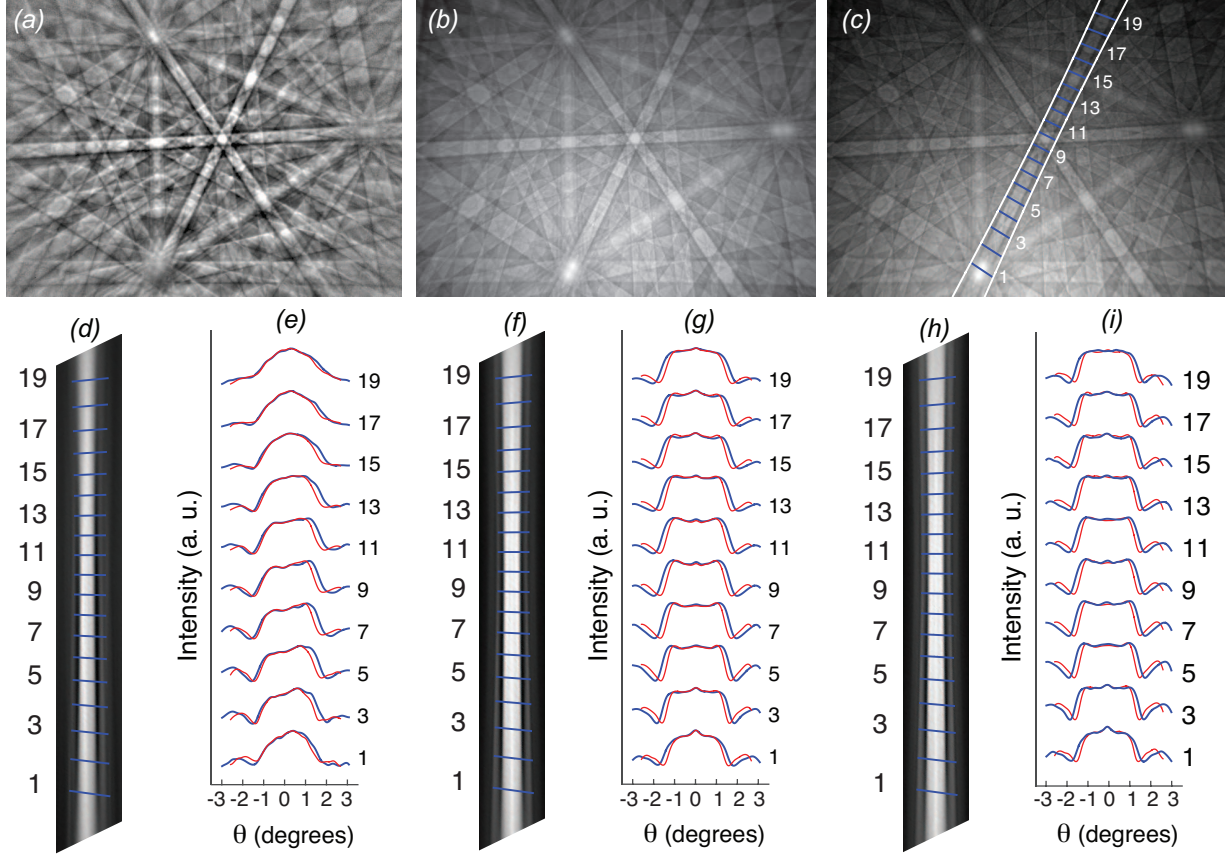
5

FIG. 3. (a) A measured EBSP generated by a 15 keV primary probe. A modeled EBSP generated by BSEs with: (b) 5 keV to 15 keV energies and (c) 15 keV energy. The Kikuchi band within the hyperbolae in (c) is extracted from all three EBSPs. The Kikuchi bands in EBSPs (a), (b) and (c) are displayed in (d), (f) and (h), respectively. The intensity profiles of these bands are plotted in (e), (g) and (i), respectively. The paths over which the intensity profiles are obtained are plotted in blue in (c). Profiles for 20 keV EBSPs are also plotted in red in (e), (g) and (i). The contrast difference between the raw (unfiltered) experimental pattern in (a) and the simulated patterns (b) and (c) is due to different intensity scaling: the simulated patterns had a gamma-correction applied to their intensity histogram to emphasize the detailed band structure.

effect is the result of a yet another anisotropy in the distribution of the inelastically scattered electrons. This anisotropy is short-range and is localized to the width of one Kikuchi band. It causes one side of a K-band to be brighter than the other side. There is a qualitative model for the excess-deficiency effect that relates it to the angular deviation of the scattered direction from the forward scattering direction (primary probe direction)[17].

(a) measured EBSD

(b) modelled EBSP
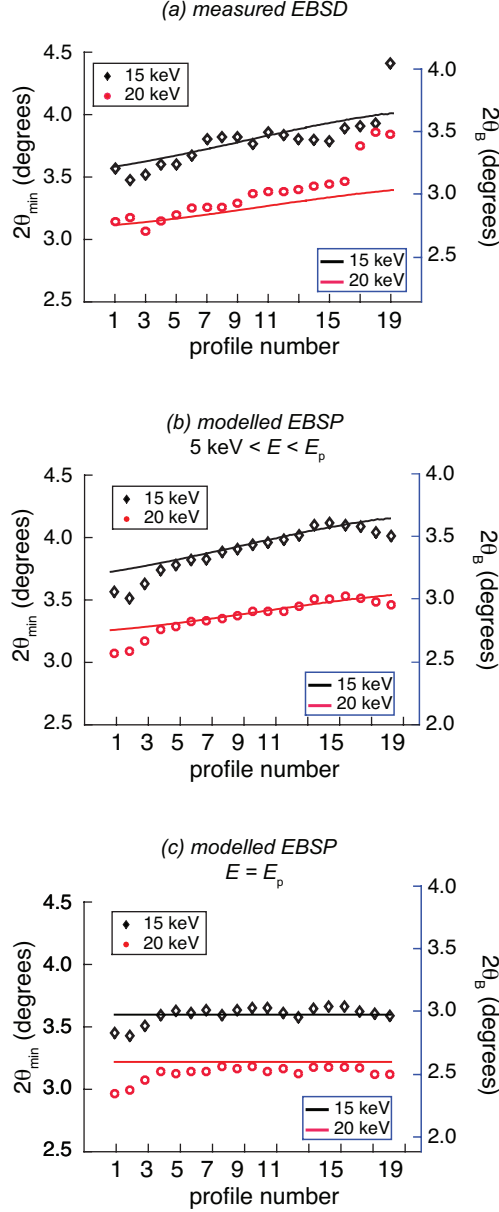5 keV < *E* < *E*$_p$

(c) modelled EBSP
E = *E*$_p$

FIG. 4. A Kikuchi band width's variation from the bottom to the top of the EBSD detector.— $2\theta_{\min}$: angular distance between the two deepest troughs on either side of an intensity profile of the {220} K-band. The data points in (a), (b) and (c) respectively correspond to the profiles in fig. 3(e), (g) and (i). The solid lines in all three graphs show the Bragg angle $2\theta_B$ of the {220} K-band. They must be read using the blue vertical axis at the right hand side of the graph. $2\theta_B$ in (a) and (b) are identical. They are obtained using the mean BSE energy of fig. 2(c). $2\theta_B$ in (c) is constant.

We define the width of a K-band as the angular distance ($2\theta_{min}$) between the two deepest troughs of an intensity profile. By comparing the K-band width of the intensity profiles it becomes evident that in all three cases (measured and modeled), the K-band width in the 20 keV EBSP (red profiles) is smaller than the K-band width in the 15 keV EBSP (blue profiles). In other words, the K-band width has decreased when the beam energy has increased. In the same manner, the decrease in the mean BSE energy from the bottom of the EBSP to its top, predicted in (fig. 2(d)), must cause the intensity profiles to be wider at the top of the EBSP.

To examine this hypothesis, we analyzed the intensity profiles of the {220} K-band more closely. In fig. 4(a), the K-band width for the profiles of fig. 3(e) are plotted. The black data points show the width of the K-band in the measured EBSP with $E_{\mathrm{p}} = 15$ keV, whereas the red data points correspond to the same K-band in the measured EBSP with $E_{\mathrm{p}} = 20$ keV. It can be clearly seen that in both cases the K-band width increases from the bottom of the EBSP to its top.

In the modeled EBSP where the lower BSE energy cut-off is 5 keV and the higher BSE energy cut-off is the primary probe energy E_{p}, the graph in fig. 4(b) shows that the variation of the width of the K-band from the bottom of the EBSP to its top is similar to that of the measured EBSP: the K-band width increases. In the single-energy modeled EBSP where $E = E_{\mathrm{p}}$, in contrast, the K-band width remains constant (fig. 4(b)) along the K-band.

The Bragg angle θ_{B} can also be obtained for each intensity profile in fig. 3. To that end, we assigned one BSE energy to each profile. This energy is the weighted average over the modeled mean BSE energies (fig. 2(c)) on the path of that profile. To obtain the Bragg angle, the modeled mean BSE energy (fig. 2(c)) is used to solve $\lambda = 2d \sin \theta_{\mathrm{B}}$; d is the interplanar spacing between two {220} planes in Silicon, and λ is the relativistic wavelength of the BSEs.

For example, when $E_{\mathrm{p}} = 15$ keV, and the included BSE energy range is 5 keV to 15 keV, on profile *11*, the modeled mean BSE energy range is 10.92 keV to 11.00 keV, which results in $1.7352° \leq \theta_B \leq 1.7419°$. To obtain the Bragg angle on path *11*, we approximate the mean BSE energy with 10.96 keV. This results in $\theta_{\mathrm{B},11} = 1.7385°$. $2\theta_{\mathrm{B}}$ values for 150 paths (including the 20 paths of fig. 3) are plotted in fig. 4; in each graph, the solid black and red curves show $2\theta_B$ for respectively $E_{\mathrm{p}} = 15 kV$ and $E_{\mathrm{p}} = 20 kV$.

In fig. 4(a) and (b), $2\theta_B$ is obtained as explained above using the modeled mean BSE

8

energy in fig. 2(c). In fig. 4(c), $2\theta_B$ is constant because the modeled EBSP is made of only BSEs with a constant energy equal to the energy of the primary probe.

Recall that in a Kikuchi band the Bragg angle does not coincide with the loci of the trough of the intensity profile. In fig. 4, we have shifted the $2\theta_B$ curves upwards with respect to the $2\theta_{min}$ scale to facilitate the comparison of the variation of $2\theta_B$ and $2\theta_{min}$. The $2\theta_B$ curves must be read using the vertical axis on the right hand side of the graph.

It can be seen in fig. 4(b) that in the modeled EBSP with BSE energies ranging from $5\,\text{keV}$ to E_p, the $2\theta_{min}$ data points are located on the vertically shifted $2\theta_B$ curves. In the measured EBSP (fig. 4(a)), there is a deviation from the shifted $2\theta_B$, which is due to the asymmetry of the intensity profiles in a measured EBSP. This asymmetry does not exist in the BSE formation model. Nevertheless, $2\theta_{min}$ closely follows the trend of the modeled $2\theta_B$ curves. In the EBSP measured with a $15\,\text{keV}$ primary probe, the K-band width increases by about $0.4°$ from the bottom of the EBSP to its top (fig. 4(a)), which is in very good agreement with the K-band width in the modeled EBSP (fig. 4(b)). We have no clear explanation for the larger deviation of $2\theta_{min}$ from the shifted $2\theta_B$ curve in profile *17-19* of the measured $20\,\text{keV}$ EBSP in fig. 4(a).

In summary, we have shown that the energy-dependence of the angular (spatial) distribution of the generated BSEs causes the width of a Kikuchi band to expand from the bottom of an EBSP to its top. In an EBSP generated with a $15\,\text{keV}$ primary probe, the K-band width varies by $0.4°$ degrees over the height of the EBSP. The K-band width variation is $0.3°$ degrees in an EBSP measured with a $20\,\text{keV}$ primary probe. We also showed that Callahan and De Graef[11]'s BSE formation model closely predicts this K-band width variation through modeling the energy-dependence of the angular (spatial) distribution of BSEs.

This relatively large K-band width variation over an EBSP has significant ramifications for EBSD geometry refinement methods as well as for those deformation retrieval methods that use modeled EBSPs. Any geometry refinement method that assumes Kikuchi band edges are hyperbolae or the Kikuchi band width is constant[1–3] must use measured EBSPs that are energy-filtered, or must explicitly take the energy variation into account. The deformation retrieval methods that obtain the deformation tensor by comparing the measured EBSP with modeled EBSPs[1,18–21] must use the modeled EBSPs that include the full BSE energy spread[11]; on the other hand, if they use single-energy modeled EBSPs, then they must use single-energy (energy-filtered) experimental EBSPs for the comparison.

---

* fram@cmu.edu

† degraef@cmu.edu

[1] C. Maurice, K. Dzieciol, and R. Fortunier, Ultramicroscopy **111**, 140 (2011).

[2] J. Basinger, D. Fullwood, J. Kacher, and B. Adams, Microscopy and Microanalysis **17**, 330 (2011).

[3] F. Ram, *the Kikuchi bandlet method for the intensity analysis of the Electron Backscatter Kikuchi Diffraction Patterns*, Ph.D. thesis, RWTH Aachen (2015).

[4] A. J. Wilkinson and D. Randman, Philosophical Magazine **90**, 1159 (2010).

[5] T. B. Britton and A. J. Wilkinson, Ultramicroscopy **111**, 1395 (2011).

[6] J. Alkorta, Ultramicroscopy **131**, 33 (2013).

[7] A. Winkelmann, C. Trager-Cowan, F. Sweeney, A. P. Day, and P. Parbrook, Ultramicroscopy **107**, 414 (2007).

[8] F. Ram, S. Zaefferer, and D. Raabe, Journal of Applied Crystallography **47**, 264 (2014).

[9] D. Joy, *Monte Carlo Modeling for Electron Microscopy and Microanalysis* (Oxford University Press, USA, 1995).

[10] H. Bethe, Ann. d. Physik **397**, 325 (1930).

[11] P. G. Callahan and M. De Graef, Microscopy and Microanalysis **19**, 1255 (2013).

[12] A. Deal, T. Hooghan, and A. Eades, Ultramicroscopy **108**, 116 (2008).

[13] A. Eades, A. Deal, A. Bhattacharyya, and T. Hooghan, in *Electron Backscatter Diffraction in Materials Science*, edited by A. J. Schwartz, M. Kumar, B. L. Adams, and D. P. Field (Springer US, Boston, MA, 2009) pp. 53–63, arXiv:arXiv:1011.1669v3.

[14] A. Winkelmann, K. Aizel, and M. Vos, New Journal of Physics **12**, 053001 (2010).

[15] S. Vespucci, A. Winkelmann, G. Naresh-Kumar, K. P. Mingard, D. Maneuski, P. R. Edwards, A. P. Day, V. O'Shea, and C. Trager-Cowan, Physical Review B **92**, 205301 (2015).

[217] [16] E. Candès and D. L. Donoho, Communications on Pure and Applied Mathematics **57**, 219 (2004).

[218] [17] A. Winkelmann, Ultramicroscopy **108**, 1546 (2008).

[219] [18] J. Kacher, C. Landon, B. L. Adams, and D. Fullwood, Ultramicroscopy **109**, 1148 (2009).

[220] [19] S. VILLERT, C. MAURICE, C. WYON, and R. FORTUNIER,
[221] Journal of Microscopy **233**, 290 (2009).

[222] [20] D. Fullwood, M. Vaudin, C. Daniels, T. Ruggles, and S. I. Wright,
[223] Materials Characterization **107**, 270 (2015).

[224] [21] B. E. Jackson, J. J. Christensen, S. Singh, M. De Graef, D. T. Fullwood, E. R. Homer, and
[225] R. H. Wagoner, Microscopy and Microanalysis **22**, 789 (2016).